Supporting Information

Dual-Function Additive Enables a Self-Regulatory Mechanism to Balance Cathode-Anode Interface Demands in Zn||MnO_2 Batteries

Yuying Han[a], Fangzheng Wang[a], Lijin Yan[a], Liang Luo[a], Yuan Qin[a], Chong Zhu[a], Jiangyu Hao[e], Qizhi Chen[d], Xuefeng Zou[c]*, Yang Zhou[b]*, and Bin Xiang[a]**

[a] College of Chemistry and Chemical Engineering, Chongqing University, Chongqing 401331, China.

[b] Analytical and Testing Center, Chongqing University, Chongqing 401331, China.

[c] Guizhou Provincial Key Laboratory of Computational Nano-Material Science, Guizhou Education University, Guiyang 550018, Guizhou, China.

[d] Guangxi Huiyuan Manganese Industry Co., Ltd, Laibin 546138, Guangxi, China.

[e] College of Chemistry and Chemical Engineering, Chongqing university of Technology, Chongqing 400054, China.

Email: xiangbin@cqu.edu.cn (B. Xiang), zhouyangyang@cqu.edu.cn (Y. Zhou), njzouxf@gznc.edu.cn (X. Zou), chenqizhi@southmn.com (Q. Chen)

1.Experimental Section

1.1. Materials

$ZnSO_4·7H_2O$, $MnSO_4$, $Na_2HPO_4·2H_2O$, N-Methylpyrrolidone (NMP) were purchased from Chengdu Kelong Chemical Co., Ltd. Polyvinylidene difluoride (PVDF) was purchased from Shanghai Xushuo Biotechnology Co., Ltd. Carbon paper was purchased from Canrd Technology Co. Ltd.

1.2 Preparation of MnO_2 electrode

The synthesis of MnO_2 was performed according to a previously reported method [1]. In brief, $KMnO_4$ (0.948 g) was dissolved in 70 ml of deionized water, 3 ml of concentrated H_2SO_4 was added slowly and stirred for 1h. The solution was transferred to a Teflon-lined autoclave and heated at 150 °C for 24 h. After cooling, the product was centrifuged several times and dried at 80 °C for 12 h.

The MnO_2 electrode was prepared by mixing MnO_2 powder, carbon black, and PVDF at a weight ratio of 7:2:1 with NMP to form a slurry. The slurry was coated onto a carbon paper and dried at 60℃ for 12 h. The mass loading of MnO_2 was approximately 2.0 mg cm^{-2}.

1.3 Preparation of batteries

The CR2032 coin cells were assembled in air with glass fiber (Whatman) as the separator, including symmetric cell, half-cells and full cell tests and 100 μl of electrolytes were added to each cell. $ZnSO_4$ (2 M) as the electrolyte for symmetric and half-cell, $ZnSO_4$ (2 M) + $MnSO_4$ (0.1 M) for full cell, 5 mmol of SDP was added as an additive to the above electrolytes, respectively. Zn plating/stripping experiments were carried out using a Zn||Zn symmetric cell. Coulombic efficiency (CE) measurements were carried out for the Zn||Cu asymmetric cells. The full cell was assembled with MnO_2 electrode as the cathode and bare Zn as the anode.

1.4 Electrochemical Measurements

All the galvanostatic charge/discharge tests were conducted on NEWARE Battery Test System (CT-4008Tn, Shenzhen China). A CHI 660E electrochemistry workstation was used to examine the EIS of the symmetrical cells in the frequency range of 0.01-100 kHz and the CV curves of the complete cells at a scan rate of 0.1 mV s^{-1}. The hydrogen evolution reaction potential was recorded using linear sweep voltammetry (LSV) method with a scan rate of 0.2 mV s^{-1} in 2 M $ZnSO_4$ electrolyte. The tafel test was carried out under three electrodes with bare Zn as the working electrodes, and Pt electrode and Ag/AgCl as the counter and reference electrodes, respectively. In-

situ pH monitor was measured on PHS-3E (Shanghai Leici) coupling a NEWARE Battery Test System (CT-4008Tn, Shenzhen China) at 10 mA cm^{-2}, and the Zn||Zn symmetrical cells were assembled in an electrolytic tank. To detect the pH near the electrode more accurately, the pH meter was placed close to the side of the preferential zinc deposition. And we fabricated a visually transparent zinc-manganese battery using a clear glass cell [2]. Carbon paper was used as the cathode substrate (led with conductive copper tape) and zinc foil (100 um thickness) was used as the anode and electrolyte, respectively. 0.1 g of bromocresol green was dissolved in 95% ethanol and diluted to 100 mL to study the in situ pH change.

Electrochemical quartz crystal microbalance (EQCM, CHI400C) was used to monitor the mass change during Zn plating/stripping, in which gold-plated quartz crystal electrode was used as the working electrode, Pt electrode was used as the counter electrode, Ag/AgCl electrode was used as reference electrode, and the EQCM test was performed by chronopotentiometry at a current of 5 mA cm^{-2}. The mass change at the quartz crystal electrode surface was calculated based on Sauerbrey equation.

$$\Delta f = -2f_o^2 \Delta m / [A \cdot \mathrm{sqrt}(\mu\rho)] \quad (1)$$

Where f_o is the basic resonant frequency of crystal (7.995MHz), A is the area of the gold plate plated on the crystal (0.196 cm^2), ρ is the crystal density (2.684g/cm^3), and μ is the crystal shear coefficient (2.947×10^{11}g /cm·s^2). The frequency change per Hertz is equivalent to 1.34 ng. The mass efficiency was defined as the ratio of the mass loss in the stripping process to the mass gain in the plating process.

1.5 Material Characterization

Environmental Scanning Electron Microscopy (ESEM, Quattro S), Energy Dispersive X-ray Spectroscopy (EDS) and Electron probe X-ray micro analyzer (EPMA, JXA-8530 Plus) were used to characterize the morphology and elemental distribution of the samples. Cross Section Polisher (CP, HITACHI Ion Milling System IM4000 II) and Hitachi Cold Field Emission Scanning Electron Microscope SU8600 were used to observe the cross-section morphology of the samples. The structure of the MnO_2 and Zn electrodes as well as the corrosion products were investigated by X-

ray diffraction (XRD, PANalytical X'Pert Powder) using Cu Kα-radiation (λ=1.5418). X-ray photoelectron spectroscopy (XPS) measurements were carried out on an ESCALAB 250 Xi X-ray photoelectron spectrometer. 3D images of the sample surface were obtained by white light interferometer (WLI, ATOMETRICS AM-7000). Dynamic contact angle testing is performed by using a contact angle meter (LAUDA Scientific GmbH, LSA-100) to observe the change in contact angle of the sample over a period of 15 minutes. The observation of dendrite growth was performed on an in situ optical microscope (WY-830S) with a specially designed electrolytic cell in a Zn||Zn symmetric configuration on the instrument. Transmission electron microscopy (TEM) and high-angle annular dark-field scanning transmission electron microscopy (HAADF-STEM), and energy-dispersive X-ray spectroscopy (EDS) mapping were conducted on a FEI Talos 200S with an operating voltage of 200 kV.

1.6 Finite Element Method Simulations

Finite element methods (FEM) conducted by COMSOL Multiphysics was used to investigate the zinc ion concentration and current distribution in different systems. Zinc ions in electrolytes were implemented by the Nernst-Plank equation. The reaction of Zn^{2+} with the Zn metal electrode was described by the Butler-Volmer equation. The FEM simulations are based on the morphology of the original zinc foil surface after CP treatment, which was calculated in a 2D region with a size of 10 x 18.5 μm^2, and a 2 x 18.5 μm^2 microzone at the electrode interface was set up close to the deposition area. The initial Zn^{2+} concentration in the electrolyte was 2.0 M. The exchange current densities of the bare Zn was 45 A m^{-2}.

1.7 Theoretical Calculations

Density generalized function theory (DFT) calculations are performed via the CASTEP module in Materials Studio software. The plane-wave energy cut-off was set to 500 eV. And the convergence criteria for geometric optimizations were set as 2×10^{-5} eV for the energy and 0.05 eV $Å^{-1}$ for the forces. To avoid the interaction between periodic slabs, a vacuum layer of about 20 Å was introduced in the perpendicular direction.

In order to investigate the mechanism of ZnPO, a superlattice structure of ZnPO was constructed and the adsorption energies of zinc ions on ZnPO and Zn(002) were calculated, and the migration energy barriers of zinc ions on ZnPO and ZHS were also compared. The adsorption energy was defined as following equation:

$$E_{aborb} = E_{total} - E_{surf} - E_{Zn} \quad (2)$$

Where E_{total}, E_{surf} and E_{Zn} correspond to the calculated total energies of the facet combined with the Zn atom, the energy of a clean surface and the energy of one Zn atom in bulk, respectively.

The diffusion reaction of Zn atom on ZnPO and ZHS activation energy (E_a) and reaction energy (E_r) were defined by Equations (3) and (4):

$$E_a = E_{TS} - E_{IS} \quad (3)$$

$$E_r = E_{FS} - E_{IS} \quad (4)$$

Where E_{IS}, E_{TS} and E_{FS} were the total energy of the initial states (ISs), transition states (TSs) and final states (FSs), respectively [3]. And structure of $ZnSO_4(OH)_6$-$4H_2O$ obtained from previous study [4].

2. Supplementary Figures and Tables

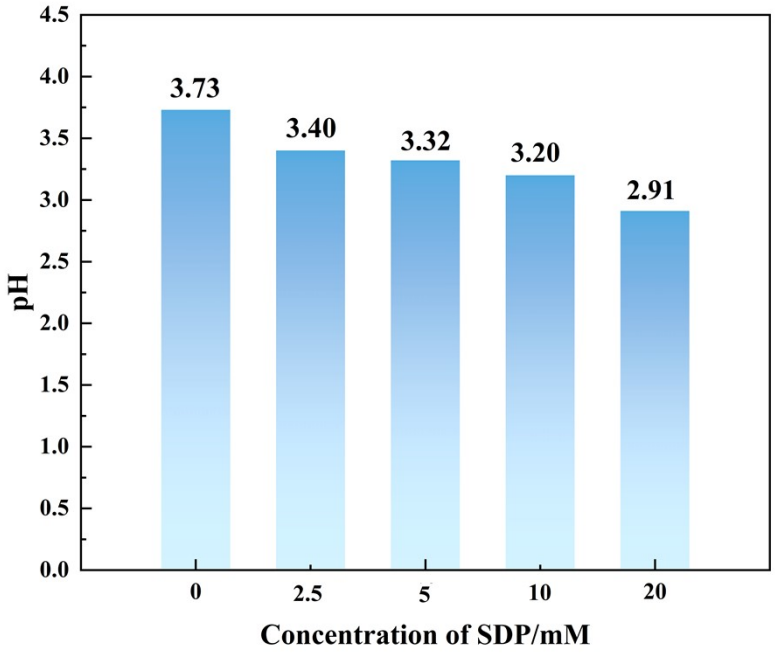

Fig. S1. pH of solutions at different SDP concentrations.

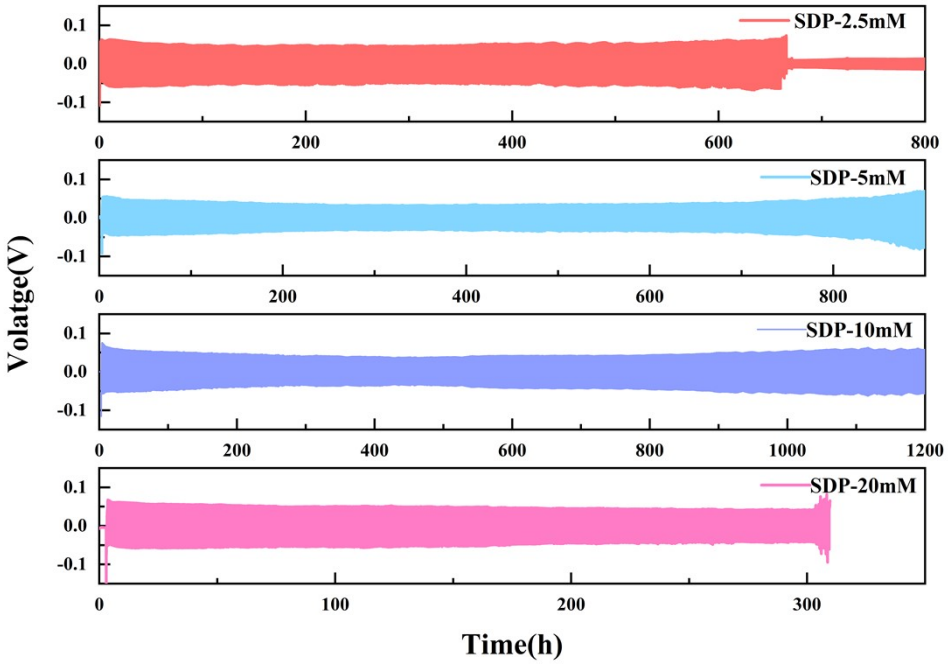

Fig. S2. Performance of Zn||Zn symmetric cells assembled at different SDP concentrations

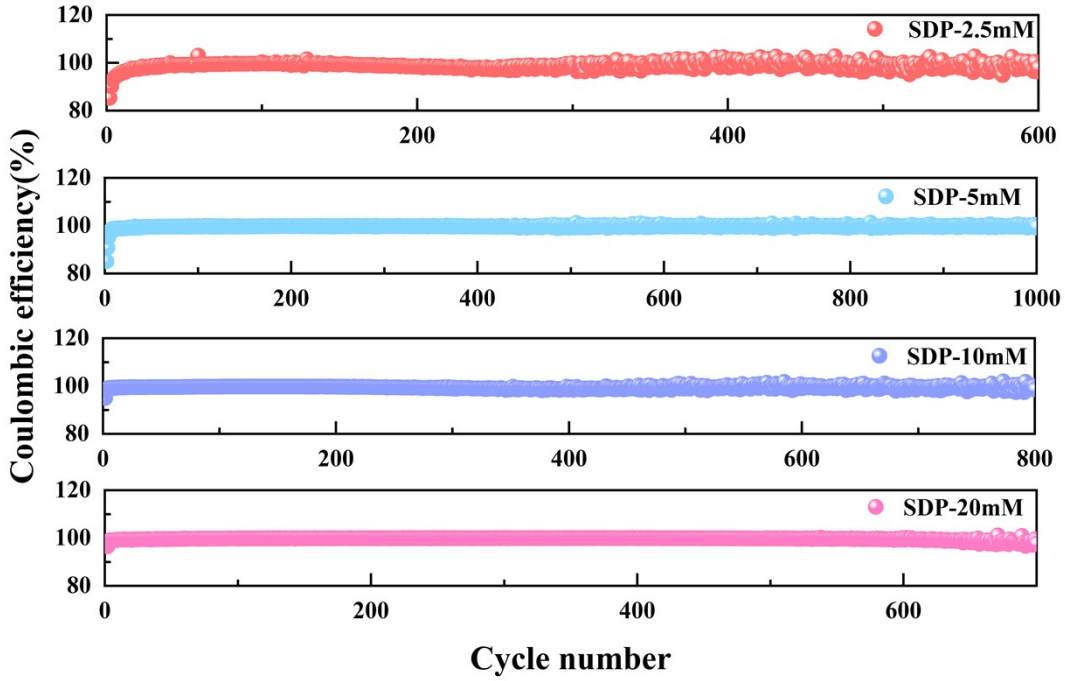

Fig. S3. Performance of Zn||Cu half-cells assembled at different SDP concentrations.

Four sets of SDP additive solutions with varying concentrations were prepared, and a gradual decrease in pH was observed as the concentration increased **(Fig. S1)**. Zn||Zn symmetric cells were assembled for long-cycle testing **(Fig. S2)**, revealing that cells with 5 mmol and 10 mmol additives exhibited longer cycle life. Specifically, the 5 mmol concentration demonstrated relatively lower polarization potential at 3 mA cm^{-2} and 1 mAh cm^{-2}. Furthermore, a Zn||Cu asymmetric cell was constructed to evaluate deposition/exfoliation performance **(Fig. S3)**. Remarkably, the 5 mmol SDP additive enabled stable cycling for 1000 cycles. This is attributed to the inability of lower SDP concentrations to form a uniform ZnPO film, while higher concentrations lead to reduced solution pH, making it prone to HER. Consequently, an appropriate SDP concentration (5 mmol) effectively enhances zinc negative electrode performance.

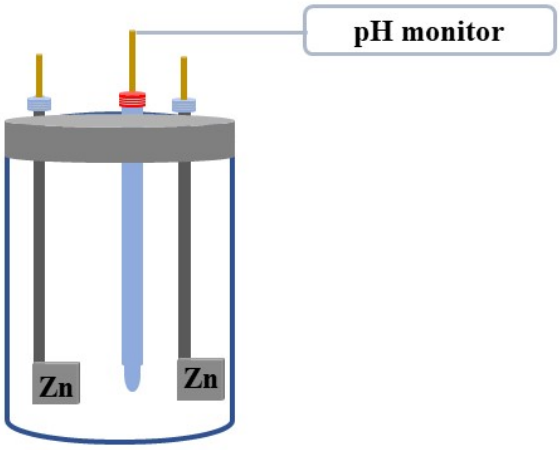

Fig. S4. Schematic diagram of an in-situ pH monitoring system.

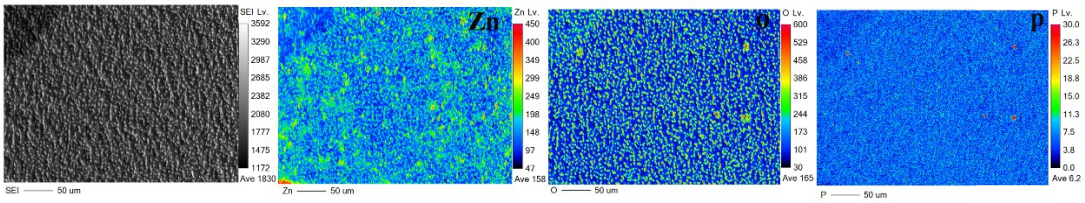

Fig. S5. EPMA elemental mappings of Cu electrode at 5 mA cm^{-2}, 1mAh cm^{-2} in completion of zinc deposition.

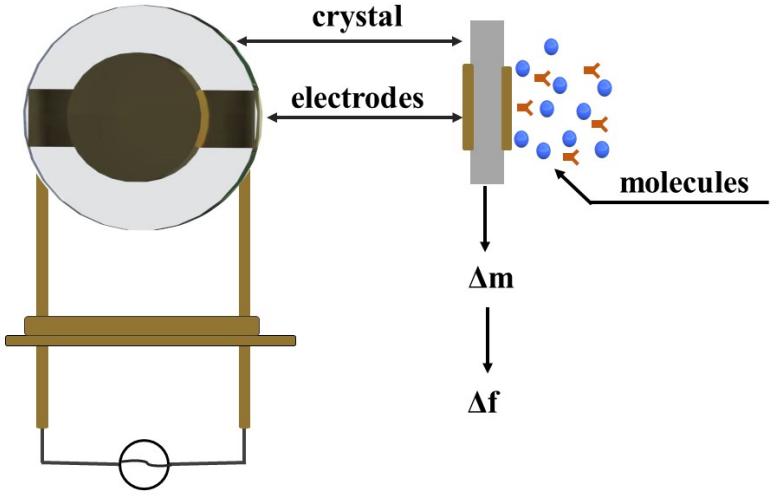

Fig. S6. Schematic diagram of the in-situ electrochemical quartz crystal microbalance (EQCM) testing.

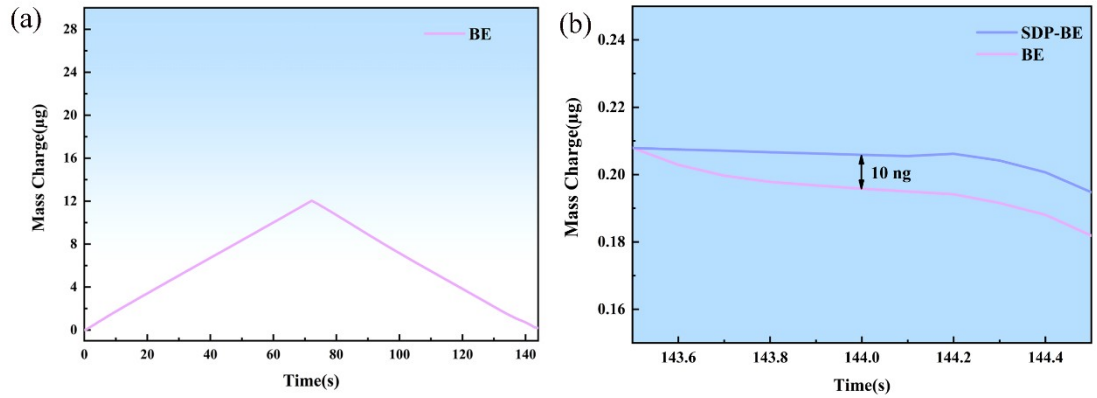

Fig. S7. Mass change in the first circle. a) Without SDP additive. b) Mass change after the first circle of stripping.

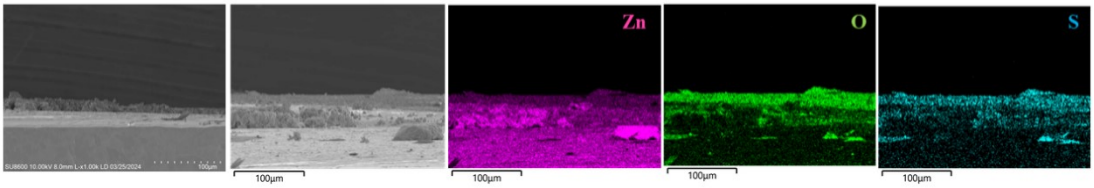

Fig. S8. Cross-section SEM image and corresponding EDS elemental mappings of Zn electrode in BE electrolytes at 1 mA cm^{-2}, 1mAh cm^{-2} after 10 cycles.

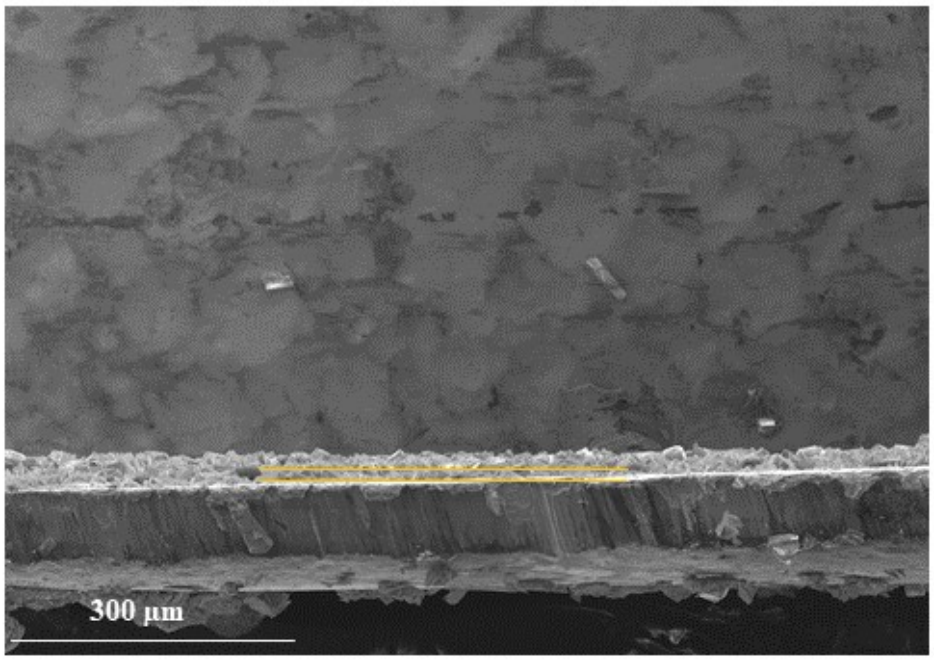

Fig. S9. Cross-section SEM image of Zn electrode in SDP-BE electrolytes at 1 mA cm^{-2}, 1mAh cm^{-2} after 10 cycles. The thickness of the SEI layer is about 25 μm.

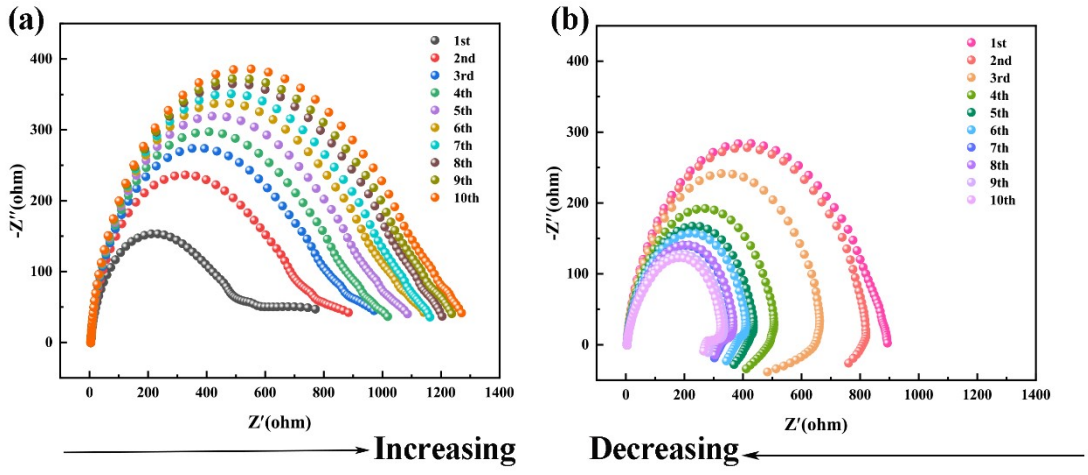

Fig. S10. In situ EIS immersed in 2M $ZnSO_4$. (a) In situ EIS immersed in 2M $ZnSO_4$+5 mM SDP.

The Zn||Zn two-electrode system was submerged in a 2M $ZnSO_4$ solution for 24 hours to conduct in-situ EIS testing. The gradual stabilization of Rct suggests the formation of a corrosion product film on the surface during the immersion period. Subsequently, the system was immersed in a solution containing 2M $ZnSO_4$ and 5 mM SDP for further in-situ EIS analysis. The gradual reduction in Rct indicates the dissolution of corrosion product adhesion due to the addition of SDP. Furthermore, the appearance of Warbug impedance in the low-frequency region with increasing immersion time indicates the generation of new substances.

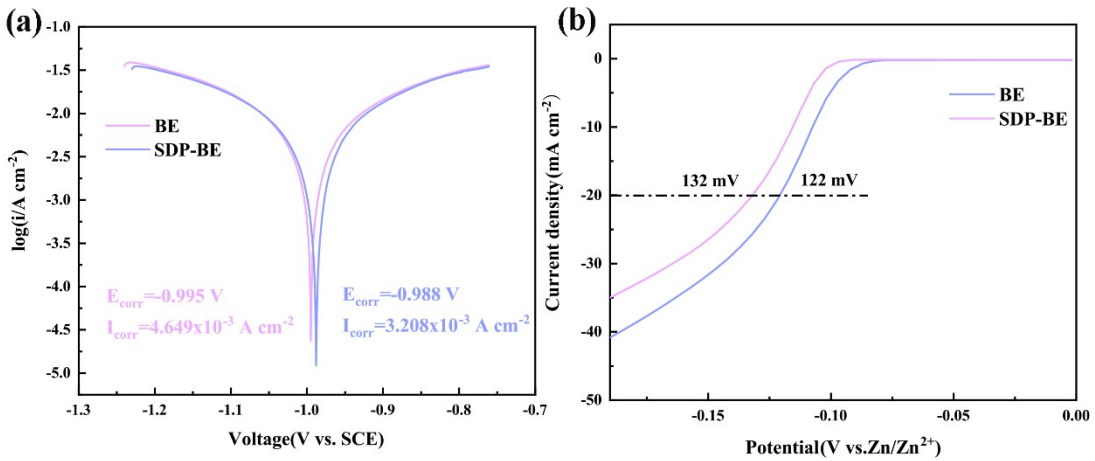

Fig. S11. (a) Linear polarization curves in BE and SDP-BE. (d) Linear sweep voltammetry (LSV) of Zn||Ti asymmetric cells.

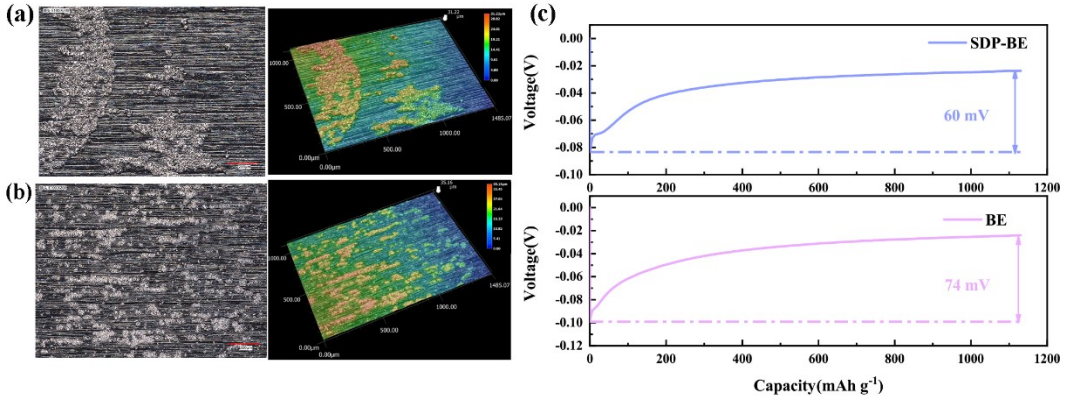

Fig. S12. 3D morphology of zinc deposition at 5mA cm^{-2}, 1mAh cm^{-2} in the electrolyte (a) without and (b) with the SDP additive. (c) Nucleation overpotentials at a current density of 1 mA cm^{-2} with/without SDP.

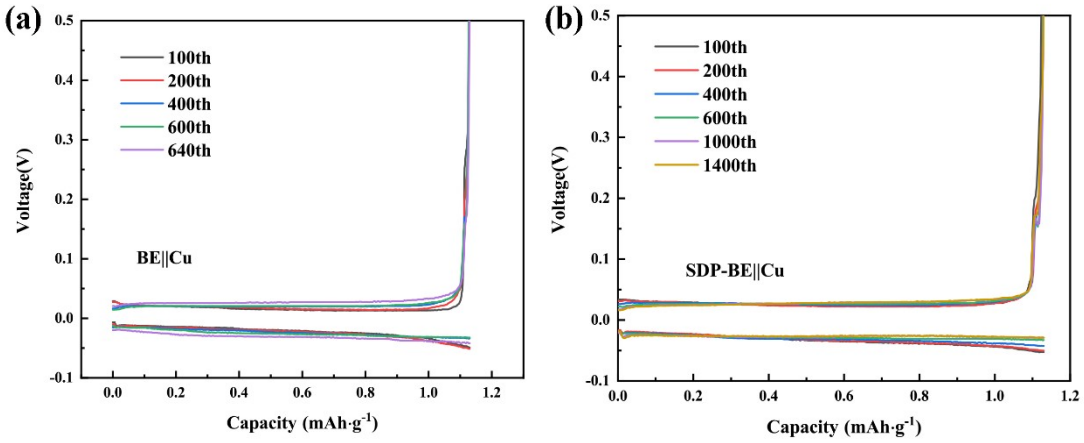

Fig. S13. Corresponding voltage distributions at different cycles in the electrolyte (a) without and (b) with the SDP additive.

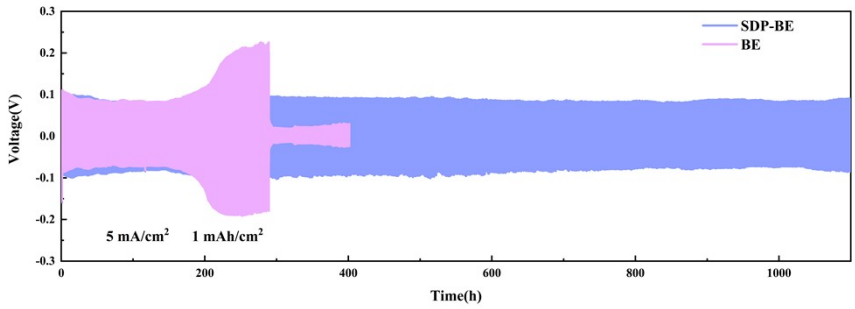

Fig. S14. Long-term galvanostatic cycling performance of Zn||Zn symmetrical batteries in electrolytes with/without SDP at 1.0 mA cm^{-2} and 1.0 mAh cm^{-2}.

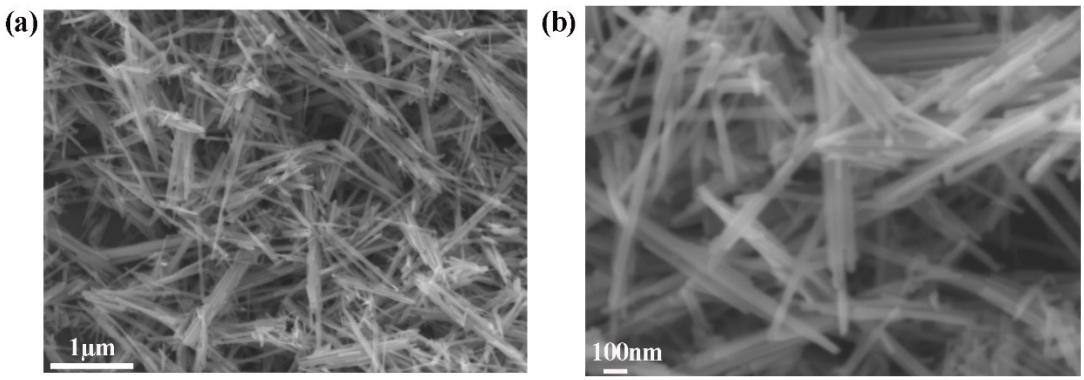

Fig. S15. SEM images of the a-MnO_2.

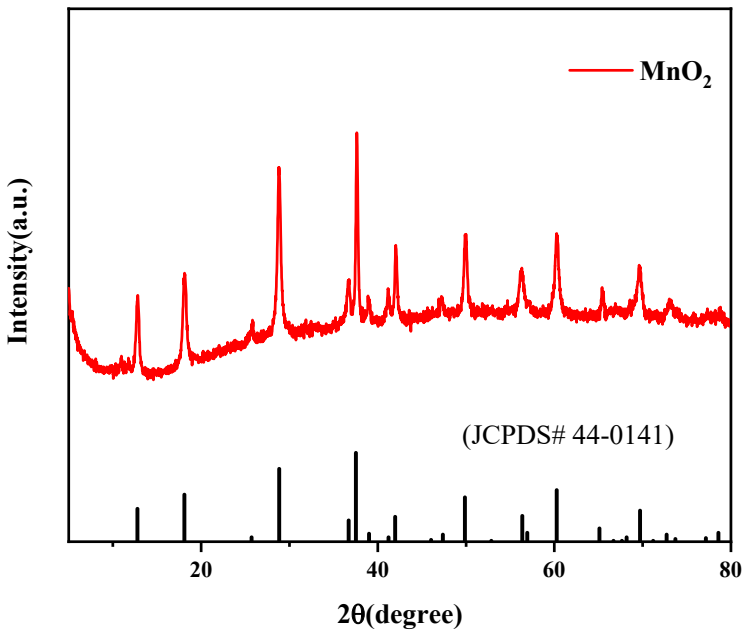

Fig. S16. XRD pattern of MnO_2 showing the α-MnO_2 structure.

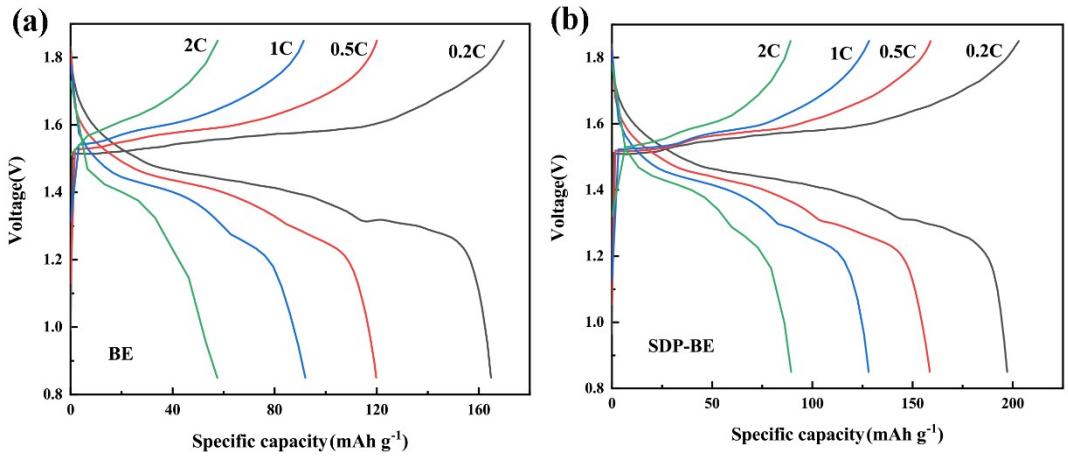

Fig. S17. Charge/discharge curves of Zn||MnO_2 cells at different multiplicities in the electrolyte (a) without and (b) with the SDP additive.

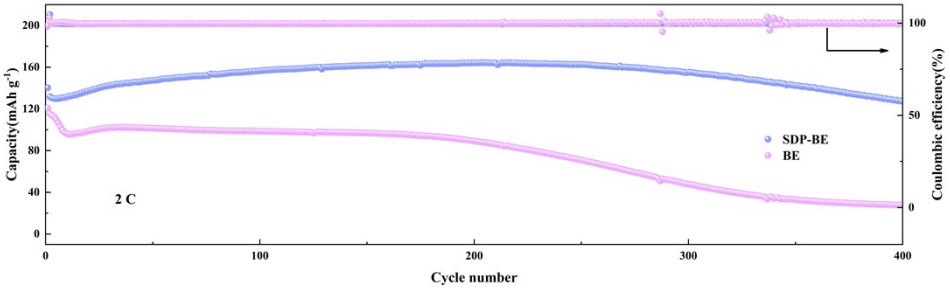

Fig. S18. Long-term cycling performance of bare Zn||MnO_2 cells at 2 C.

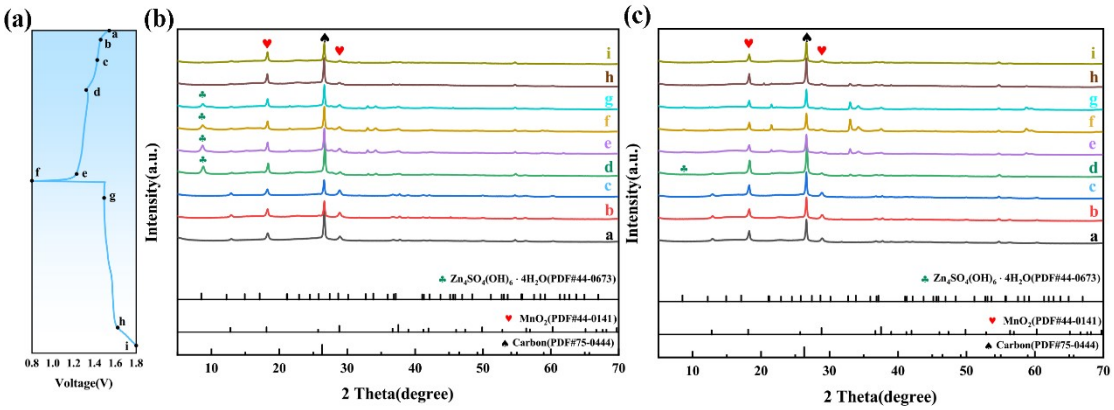

Fig. S19. The galvanostatic charge/discharge curves and ex-situ XRD patterns of the a-MnO_2 electrode during the initial first cycles. (a) GCD curves. (b) XRD patterns of BE sample. (c) XRD patterns of SDP-BE sample.

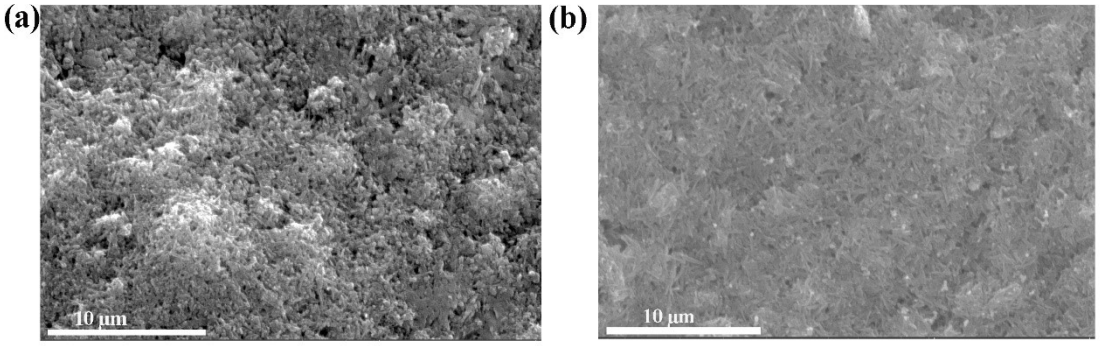

Fig. S20. SEM images of the MnO_2 electrode after three cycles in the electrolyte (a) without and (b) with the SDP additive.

Table S1. Performance comparison of SDP additive strategies between this work and other reported studies.

Strategy	Current density (mA cm-2)	Capacity (mAh cm-2)	Cycle time (hour)	Reference
Zn@ZnPO	5	1	1976	1[5]
ZnPO@Zn	2	2	920	2[6]
Zn(002)@ZPO	1	1	3599	3[3]
DTPMP-Zn	1	0.5	1100	4[7]
	5	0.5	1300	
Zn|In	0.2	0.2	1500	5[8]
Zn@Ag	0.25	0.5	1750	6[9]
MZn-60	0.2	0.2	800	7[10]
$ZnSO_4$ with 20 DMSO	1	1	2100	8[11]
67Malt/ZS	1	0.5	1200	9[12]
$ZnSO_4$+PGA	2	1	1650	10[13]
L-CN/ZnSO4	8.85	8.85	980	11[14]
$ZnSO_4$/TXA	5	5	700	12[15]
MPVMT@Zn	1	1	2000	13[16]
	5	5	680	
Tris/$ZnSO_4$	3	1	2500	14[17]
SDP-BE	1	1	3000	This work
	5	1	1100	

3. Reference

[1] S. Cui, D. Zhang, G. Zhang, Y. Gan, *J. Mater. Chem. A* 2022, 10, 25620.

[2] J. Wu, Y. Tang, H. Xu, G. Ma, J. Jiang, C. Xian, M. Xu, S.-J. Bao, H. Chen, *Nano-Micro Lett.* 2024, 16.

[3] X. Song, L. Bai, C. Wang, D. Wang, K. Xu, J. Dong, Y. Li, Q. Shen, J. Yang, *Acs Nano* 2023, 17, 15113.

[4] D. Wang, D. Lv, H. Peng, N. Wang, H. Liu, J. Yang, Y. Qian, *Nano Lett.* 2022,22,1750.

[5] S. Zhang, M. Ye, Y. Zhang, Y. Tang, X. Liu, C. C. Li, *Adv. Funct. Mater.* 2023, 33.

[6] S. Xia, Q. Luo, J. Liu, X. Yang, J. Lei, J. Shao, X. Tang, *Small* 2024.

[7] H. Yu, Y. Chen, W. Wei, X. Ji, L. Chen, *Acs Nano* 2022, 16, 9736.

[8] D. Han, S. Wu, S. Zhang, Y. Deng, C. Cui, L. Zhang, Y. Long, H. Li, Y. Tao, Z. Weng, Q.-H. Yang, F. Kang, *Small* 2020, 16.

[9] Y. Wang, Y. Chen, W. Liu, X. Ni, P. Qing, Q. Zhao, W. Wei, X. Ji, J. Ma, L. Chen, *J. Mater. Chem. A* 2021, 9, 8452.

[10] N. Zhang, S. Huang, Z. Yuan, J. Zhu, Z. Zhao, Z. Niu, *Angew. Chem., Int. Ed.* 2021, 60, 2861.

[11] D. Feng, F. Cao, L. Hou, T. Li, Y. Jiao, P. Wu, *Small* 2021, 17.

[12] W. Chen, S. Guo, L. Qin, L. Li, X. Cao, J. Zhou, Z. Luo, G. Fang, S. Liang, *Adv. Funct. Mater.* 2022, 32.

[13] C. Huang, J. Mao, S. Li, W. Zhang, X. Wang, Z. Shen, S. Zhang, J. Guo, Y. Xu, Y. Lu, J. Lu, *Adv. Funct. Mater.* 2024.

[14] H. Yu, D. Chen, X. Ni, P. Qing, C. Yan, W. Wei, J. Ma, X. Ji, Y. Chen, L. Chen, *Energy Environ. Sci.* 2023, 16, 2684.

[15] J. Yin, H. Liu, P. Li, X. Feng, M. Wang, C. Huang, M. Li, Y. Su, B. Xiao, Y. Cheng, X. Xu, *Energy Storage Materials* 2023, 59.

[16] Z. Zheng, X. Zhong, Q. Zhang, M. Zhang, L. Dai, X. Xiao, J. Xu, M. Jiao, B. Wang, H. Li, Y. Jia, R. Mao, G. Zhou, *Nat. Commun.* 2024, 15.

[17] M. Han, J. Zhang, C. Yu, J. Yu, Y. Wang, Z. Jiang, M. Yao, G. Xie, Z. Yu, J. Qu, *Angew. Chem., Int. Ed.* 2024.